

Influence of Lubricants on Wear and Self-Lubricating Mechanisms of Ni₃Al Matrix Self-Lubricating Composites

Jie Yao, Xiaoliang Shi, Wenzheng Zhai, Zengshi Xu, Ahmed Mohamed Mahmoud Ibrahim, Qingshuai Zhu, Yecheng Xiao, Long Chen, and Qiaoxin Zhang

(Submitted March 12, 2014; in revised form May 30, 2014; published online October 11, 2014)

A research is conducted on the possible beneficial synergistic effects of multiple additives in self-lubricating composites for use in high temperature friction and wear-related mechanical assemblies. Dry sliding tribological tests of Ni₃Al matrix self-lubricating composites (NMSCs) on a HT-1000 ball-on-disk high-temperature tribometer are undertaken against Si₃N₄ at 25–800 °C. The results show that the subsurface microstructures beneath wear scar of NMSCs change with addition of different lubricants, which have great effects on tribological mechanisms and tribological performances. NMSC with addition of MoS₂ and Ti₃SiC₂ exhibits distinct subsurface microstructure beneath wear scar and excellent tribological performance among all samples.

Keywords friction coefficient, metal matrix composites, microstructure, wear mechanism, wear resistance

1. Introduction

Searching high-temperature self-lubricating composites has been driven by the demand put forth by the advanced technological systems like high-performance gas turbine engines and aerospace applications in which the tribological components are supposed to have good tribological behaviors from room temperature (RT) to high temperature (Ref 1). High-temperature self-lubricating composites with good wear resistance or excellent antifricition have been developed from RT to high operating temperatures in many tribological systems (Ref 2, 3). However, self-lubricating composites with both high wear resistance and low friction remain great challenge for today's moving mechanical assemblies. Since the first studies of tribological properties of Ni₃Al-based intermetallic alloys, a wide variety of researches have been carried out to describe and summarize the wear mechanisms during the sliding friction processes (Ref 4–6). Gong et al. (Ref 5) have investigated the wear behavior of an iron-alloyed Ni₃Al with 6 vol.% Cr₃C₂ particles and 6 vol.% MnS particles. The results of friction and wear tests show that the Ni₃Al-based alloy exhibits a relatively low friction coefficient of 0.32 ± 0.02 under 20 N and its wear rate is reduced to $7.62 \times 10^{-5} \text{ mm}^3 \text{ N}^{-1} \text{ m}^{-1}$ under a higher load of 40 N. La et al. (Ref 6) have examined the tribological properties of Ni₃Al-Cr₇C₃ composite coating under water lubrication. In addition, the effects of load and sliding speed on wear rate of the coating are investigated as well. The acting

wear mechanism of the coating is plastic deformation at load of 80 N and sliding speed of 0.05 m s^{-1} . However, the wear mechanism transforms to microfracture and microplowing at high load with low sliding speed, and oxidation wear at high sliding speed. In these studies, the composites, consisting of Ni₃Al matrix with chromium or chromium compounds additions as reinforcing phase, exhibit low friction coefficients and wear rates.

Taking into account the excellent high temperature performance and the potential applications in the field of tribology of Ni₃Al-based intermetallic alloys, several lubrication phases have been selected to prepare Ni₃Al self-lubricating composites for in-depth study. Zhu et al. (Ref 7) have studied the sliding wear properties of Ni₃Al-BaF₂-CaF₂-Ag-Cr against Si₃N₄ ceramic ball. They found that the low friction coefficient of the Ni₃Al self-lubricating composite was a result of the favorable mechanical strength and the synergistic effects of Ag, fluorides, and chromates formed in the tribo-chemical reaction at high temperatures; the low wear rate might be attributed to the high strength and the excellent lubricating properties of the composite. Zhang et al. (Ref 8) have investigated the high-temperature dry sliding tribological properties of Ni₃Al-hBN-Ag composite coating in air. The results showed that the coating possesses self-lubricating properties from room temperature to 800 °C were due to a synergetic lubricating action of Ag and hBN.

Although most prepared self-lubricating composites have shown good tribological properties and the wear mechanisms and self-lubricating mechanisms have been investigated, the actions of lubricants on tribological mechanisms should be further researched.

Ti₃SiC₂ has been proved to be promising tribological material as an additive to the self-lubricating composites (Ref 9–11). In our previous study (Ref 12), it is reported that Ti₃SiC₂ as solid lubricant in NiAl alloys can promote the strength and improve tribological performances of NiAl matrix self-lubricating composites effectively at high temperatures. Moreover, Ag and hexagonal boron nitride (hBN) as lubricants have been reported to improve the tribological properties at

Jie Yao, Xiaoliang Shi, Wenzheng Zhai, Zengshi Xu, Ahmed Mohamed Mahmoud Ibrahim, Qingshuai Zhu, Yecheng Xiao, Long Chen, and Qiaoxin Zhang, School of Mechanical and Electronic Engineering, Wuhan University of Technology, 122 Luoshi Road, Wuhan 430070, China. Contact e-mail: sx1071932@126.com.

elevated temperature (Ref 13). MoS₂ as solid lubricant has been extensively studied (Ref 14-16). The results show that MoS₂ can work well at low temperatures, especially in vacuum, but it can be easily oxidized at high temperatures. Hence, MoS₂ is often selected as solid lubricant at low temperatures.

Based on the reported advantages/disadvantages of these aforementioned lubricants, we intend to design the tribological performance of Ni₃Al matrix self-lubricating composites (NMSCs) with both high wear resistance and low friction coefficient, and investigate the corresponding wear and lubricating mechanisms. For validating our ideas, the Ni₃Al (NT), Ni₃Al-Ag-Ti₃SiC₂ (AT), Ni₃Al-MoS₂-Ti₃SiC₂ (MT), Ni₃Al-MoS₂-ZnO (MZ) composites are fabricated using spark plasma sintering (SPS). The detailed discussion of the wear and lubricating mechanisms of NMSCs from 25 to 800 °C are carried out.

2. Experimental

2.1 Material Processing

In this study, the powder metallurgy technique using SPS was utilized in order to produce the NMSCs. The compositions of the sintered samples are listed in Table 1. The composite powders of Ni₃Al matrix consist of commercially available Ni, Al, Cr, Mo, Zr, and B powders (30-50 μm in average size, 99.9 wt.% purity) by atomic ratio of 4.5Ni: 1Al: 0.333Cr: 0.243Mo: 0.0047Zr: 0.0015B. The fabrication process of Ti₃SiC₂ powder (5 μm in average size, 95.0 wt.% purity) in our lab was described in detail (Ref 17). The average grain sizes of Ag, ZnO, and MoS₂ powders were about 20-40 μm. Before commencing the SPS process, the raw powders were mixed by high-energy ball-milling for 12 h with the milling speed of 200 rpm in vacuum. Balls and vials were made of hard alloy, and the charge ratio (ball to powder mass ratio) employed was 10:1. After being mixed and dried, the mixtures were then sintered by SPS using a D.R.Sinter[®] SPS3.20 (Sumitomo Coal & Mining, now SPS Syntex Inc.) apparatus at 1100 °C under a pressure of 40 MPa for 5 min in pure Ar atmosphere protection. The heating rate was 100 °C min⁻¹. The cylindrical graphite molds with an inner diameter of 20 mm were used. The as-prepared specimen surfaces were ground to remove the layer on the surface and polished mechanically with emery papers down to 1200 grit, and then with 0.05 μm wet polishing diamond pastes. Before tribological tests, the Vickers hardness of each as-received specimen was measured, according to the ASTM standard E92-82 (Ref 18), using a HVS-1000 Vickers hardness instrument with a load of 9.8 N and a dwell time of 10 s. Ten tests were conducted and the mean value was obtained. Elastic modulus were calculated from the load and depth dates obtained by nanoindentation in the specimens at peak indentation load of 8000 μN using a nanomechanical test instrument (HYSITRON, INC.).

Table 1 The chemical compositions and mechanical properties of NMSCs

Specimen	Composition, wt. %	Hardness, GPa	Elastic modulus, GPa
NT	Ni ₃ Al	4.7	143
AT	Ni ₃ Al + 7.5% Ag + 7.5% Ti ₃ SiC ₂	7.1	184
MT	Ni ₃ Al + 7.5% MoS ₂ + 7.5% Ti ₃ SiC ₂	7.9	211
MZ	Ni ₃ Al + 7.5% MoS ₂ + 7.5% ZnO	5.2	156

2.2 Friction and Wear Test

The dry sliding friction and wear tests were conducted on a HT-1000 ball-on-disk high-temperature tribometer (made in Zhong Ke Kai Hua Corporation, China) according to the ASTM Standard G99-95 (Ref 19). The disc samples (diameter of 20 mm, height of 5 mm) of NMSCs were rotated and slid against a stationary ball slider of 6 mm diameter under a contact load of 10 N. The selected test temperatures were 25 (RT), 200, 400, 600, and 800 °C. The sliding speed was 0.20 m s⁻¹. The friction radius was 2 mm. The testing time was 80 min. The counterface ball was commercially available Si₃N₄ ball (15 GPa) with surface roughness (*R_a*) of 0.01 μm. The friction coefficient was automatically measured and recorded in real time by the computer system of the friction tester. The profile of worn surface was measured using a surface profilometer. The wear volume was determined as $V = AL$, where A is the cross-section area of worn scar, and L is the perimeter of the worn scar. The wear results obtained during this work have been presented in terms of specific wear rate which was calculated as follows (Ref 20):

$$\text{specific wear rate} = V/PL, \quad (\text{Eq 1})$$

where V is the worn volume in mm³, P is the normal load in N, and L is the sliding distance in mm. All the tribological tests were carried out at least three times to make sure the reproducibility of the experimental results in the same conditions, and the average results were reported.

2.3 Microstructural Examination

The surfaces of the as-prepared specimens were examined by x-ray diffraction (XRD) analysis with CuK_α radiation at 30 kV and 40 mA at a scanning speed of 0.01°s⁻¹ for the identification of the phase constitution. The microstructures of NMSCs were analyzed using electron probe microanalysis (EPMA, JAX-8230) and energy dispersive spectroscopy (EDS, GENESIS 7000). The morphologies and compositions of worn surfaces of NMSCs were examined using electron probe microanalysis (EPMA, JAX-8230) and energy dispersive spectroscopy (EDS, GENESIS 7000). The microstructures and morphologies of cross-sections of wear scars were observed by a scanning electron microscope (SEM, JSM-5610LV) attached with EDS (GENESIS 7000).

3. Results

3.1 Mechanical and Microstructural Properties

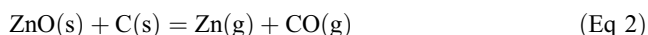
For determining the phase constitution of the as-prepared specimens, XRD patterns of NMSCs with various lubricants are shown in Fig. 1. As shown in Fig. 1(a), the main phase of NT is Ni₃Al. Additionally, C phase also appears, indicating that carburization has occurred during the SPS process. Moreover,

two new phases, TiC and Al₂O₃, can be seen to appear in the XRD patterns of AT (see Fig. 1b), MT (Fig. 1c), and MZ (Fig. 1d). It can be concluded that possible solid-state reactions between Ni₃Al and Ti₃SiC₂, ZnO, C, MoS₂ occur during the fabrication process. For the impurity of Ti₃SiC₂ lubricant, the Ti and C phases could be existed in the initial powders. Hence, in order to explain the final reaction synthesis compounds of TiC and Al₂O₃, it is necessary to list the possible reactions and calculate their Gibbs free energy. The change of Gibbs free energy ΔG° (kJ mol⁻¹) for reaction is as follows:



$$\Delta G_1^\circ = -184.80 + 15.55 \times 1423/1000 = -162.67 < 0$$

Herein, the formation of TiC could be occurred during the sintering process. The reactions between ZnO and C phases should be described as follow:



A small amount of CO(g) could be produced in the process of carbothermal reduction of ZnO, and would carry reactions with the gaseous Al(g). The production of Al₂O₃ could proceed during the temperature was above 673 K (Ref 21). Hence, the above thermodynamic analysis results indicate the reaction synthesis of stable compounds Al₂O₃ and TiC, which is confirmed by the XRD patterns of NMSCs shown in Fig. 1. TiC and Al₂O₃ can enhance the wear resistance of the composites effectively (Ref 22, 23).

Since wear has been traditionally linked to hardness, the hardness and elastic modulus of the samples are investigated by hardness and nano-indentation tests. As shown in Table 1, AT, and MT compared with NT (Ni₃Al based alloy) exhibit higher Vickers hardness and elastic modulus. Representative load-depth plots of nanoindentations made at 8000 μN indentation load are compared in Fig. 2. As shown in Fig. 3(a)-(d), the indentation depths in NT (300 nm), AT (240 nm), MT (215 nm), and MZ (275 nm) are obviously different from the results of nanoindentations. The depth of MT shows the

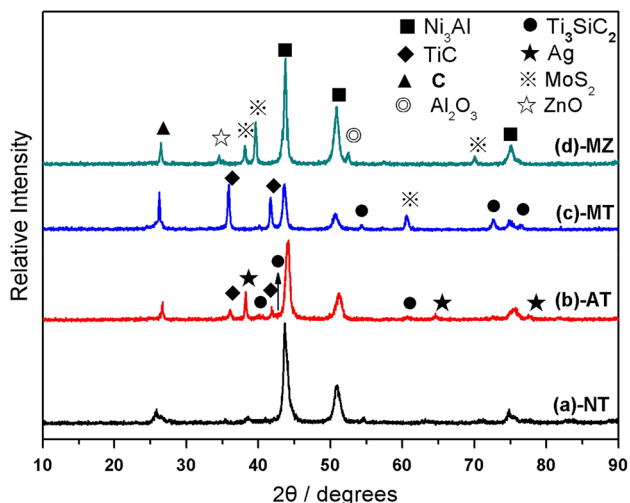


Fig. 1 XRD patterns of the NT, AT, MT, and MZ

shallowest indentation, suggesting that MT exhibits higher hardness and elastic modulus. Moreover, the total penetration depth into NT is around 300 nm, which states that the hardness of NT should be lower than that of the AT, MT and MZ. Apparently, the addition of Ti₃SiC₂ improves the hardness and elastic modulus of the monolithic Ni₃Al. In our previous study (Ref 12), the composite with the addition of Ti₃SiC₂ has higher mechanical properties compared to NMSC without Ti₃SiC₂ addition. Furthermore, the Al₂O₃ formed during the fabrication process also can enhance the hardness. MZ also has higher hardness compared to NT. It is obvious that the addition of lubricants could enhance the mechanical properties of NMSC. The higher Vickers microhardness of the NMSC could lead to better mechanical and tribological properties.

As shown in Fig. 3, the AT, MT, and MZ, free from microcracks and pores, have a uniform and dense microstructure predominantly consisting of the primary Ni₃Al alloy and lubrication phases. For AT, EDS analysis indicates that the white area is Ag-rich phase while the gray area is Ti₃SiC₂-rich phase (see Fig. 3a). For MT, EDS analysis indicates that the gray area is Ti₃SiC₂-rich phase and the black area is MoS₂-rich phase (see Fig. 3b). For MZ, the white area is ZnO-rich and Al₂O₃-rich phases while the black area is MoS₂-rich phase (see Fig. 3c).

3.2 Tribological Performance of NMSCs

Figure 4(a) shows the variations in friction coefficients of NT, AT, MT, and MZ against Si₃N₄ balls at different temperatures under an applied load of 10 N. It can be seen that the friction coefficient of NT at room temperature is relatively high, i.e. about 0.69. As the temperature increases from RT to 800 °C, the friction coefficient of NT decreases slightly from 0.69 to 0.45. The friction coefficients of MZ are smaller than that of NT throughout the test temperatures and in the range of 0.38-0.55. AT and MT have lower friction coefficient compared to NT and MZ. In addition, the friction coefficients of AT and MT exhibit downward trend from 200 to 600 °C; while the upward trend for all samples are observed when the temperature is raised above 600 °C. The fluctuations of friction coefficients, as can be seen from the error bar, are higher for the NT and AT, if compared to that of the MT and MZ.

Figure 4(b) shows the variation of wear rates of samples at different temperatures. For NT, the wear rate reaches its minimum value of $2.6 \times 10^{-5} \text{ mm}^3 \text{ N}^{-1} \text{ m}^{-1}$ at 600 °C and increases as the temperature increases to 800 °C. It can be found that the wear rates of MT and MZ decrease sharply from RT to 400 °C and continue to decline slowly up to 800 °C. As the temperature increases from RT to 800 °C, the wear rates of AT decrease from 4.5 to $1.8 \times 10^{-5} \text{ mm}^3 \text{ N}^{-1} \text{ m}^{-1}$, except for the wear rate at 600 °C, which is higher than that at 400 and 800 °C. The reason for the relatively high wear rate at 600 °C is investigated in discussion in detail. As the temperature increases to 200 °C, the MT and MZ show a comparable wear rate of about $2.0 \times 10^{-5} \text{ mm}^3 \text{ N}^{-1} \text{ m}^{-1}$. The wear rates of MT are lower from 400 to 800 °C, if compared to that of the MZ. At 800 °C, the MT exhibits excellent wear resistance, and the wear rate is about $0.8 \times 10^{-5} \text{ mm}^3 \text{ N}^{-1} \text{ m}^{-1}$. The fluctuations of wear rates, as can be seen from the error bar, are higher for the NT and AT, if compared to that of the MT and MZ.

Apart from the lubrication for NMSCs, the wear of counterface balls can also be decreased with the addition of

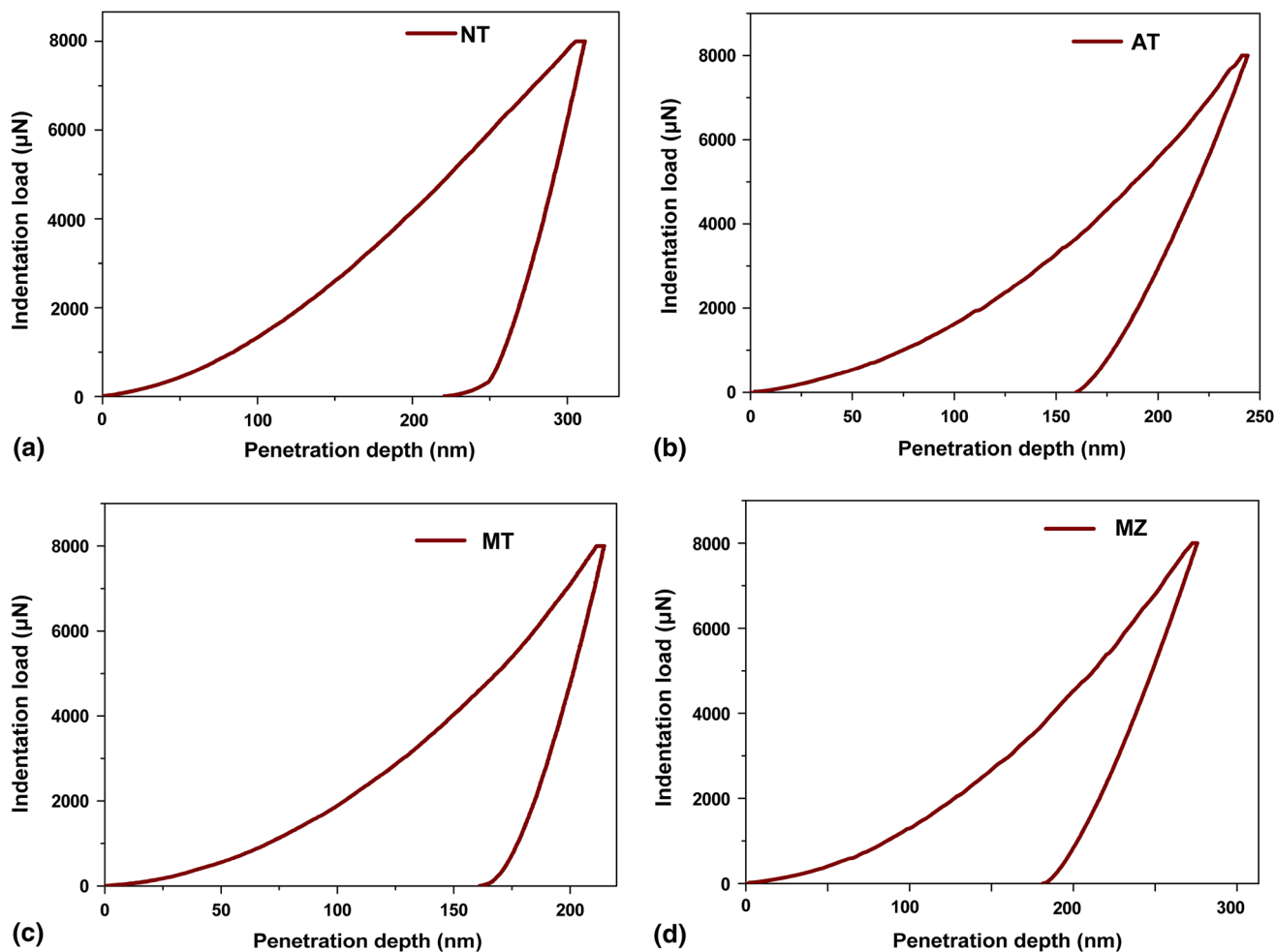


Fig. 2 Representative load-depth plots of nanoindentations in NT (a); AT (b); MT (c); and MZ (d)

lubricants. Figure 4(c) shows the variation of wear rates of counterface balls at different temperatures. The decreasing tendency of wear rate of counterface balls with the increase in temperature has been observed. The Si_3N_4 counterface ball sliding against MT shows the relative low wear rates of $0.86\text{--}2.44 \times 10^{-5} \text{ mm}^3 \text{ N}^{-1} \text{ m}^{-1}$ from RT to 800°C , if compared to the Si_3N_4 balls sliding against NT, AT, and MZ.

From the above tribological results, it can be found that the friction coefficients and wear rates of AT, MT, and MZ have been reduced by adding lubricants. Additionally, the MT with low friction coefficients of 0.26–0.34 and wear rates of $0.8\text{--}3.7 \times 10^{-5} \text{ mm}^3 \text{ N}^{-1} \text{ m}^{-1}$ shows the excellent self-lubricating performance among the NMSCs in the range of $25\text{--}800^\circ\text{C}$. Furthermore, at 600°C , all the AT, MT, and MZ show the lowest friction coefficients over the temperature range of $25\text{--}800^\circ\text{C}$.

3.3 Morphologies of Worn Surfaces

Figure 5 shows the wear track morphologies of NT tested at different temperatures. The slight scratches and potholes on the smooth worn surface in Fig. 5(a) suggest that the main wear mechanisms are microplowing and microcutting at RT. The size and amount of scratches and potholes decrease with increase in temperature, suggesting that the main wear mechanisms are microcutting at 200 and 400°C (see Fig. 5b, c). At 600°C ,

local deformations and loose wear debris are found in some spots of the worn surface (see Fig. 5d), and the main wear mechanism is plastic deformation. When the temperature rises to 800°C , it can be seen from Fig. 5(e) that deep grooves with plowing are much more obvious and the sliding surface of NT is sheared and plowed off by the Si_3N_4 ceramic ball due to the decrease in strength. The same phenomenon has been also observed by Zhu et al. (Ref 7). The main wear mechanism is transformed from microcutting to microplowing.

Figure 6 shows the wear track morphologies of AT tested at different temperatures. As shown in Fig. 6(a), deep grooves are found on the worn surface, indicating that the main wear mechanism is microplowing. Compared with NT, the decrease in friction coefficient of AT at RT can be attributed to the lubricating nature of Ag. According to the EDS analysis, the area with more grooves is Ag-rich phase, whose composition is Ni42.93–Al12.22–Ag37.93–O2.38–Si0.65–Ti1.26–C0.72–Mo13.11 (in wt.%). When the temperature rises to 200°C , the worn track of AT is found to be much smoother, if compared to that at RT. Fine grooves and plastic flow indicate that the wear mechanism is mostly microplowing and plastic deformation at 200°C . At 400°C , delamination pits and coarse grooves are found on the worn surface, indicating that the wear mechanism is transformed from microplowing to delamination. A lower friction coefficient could be attributed to the effectiveness of Ag in reducing

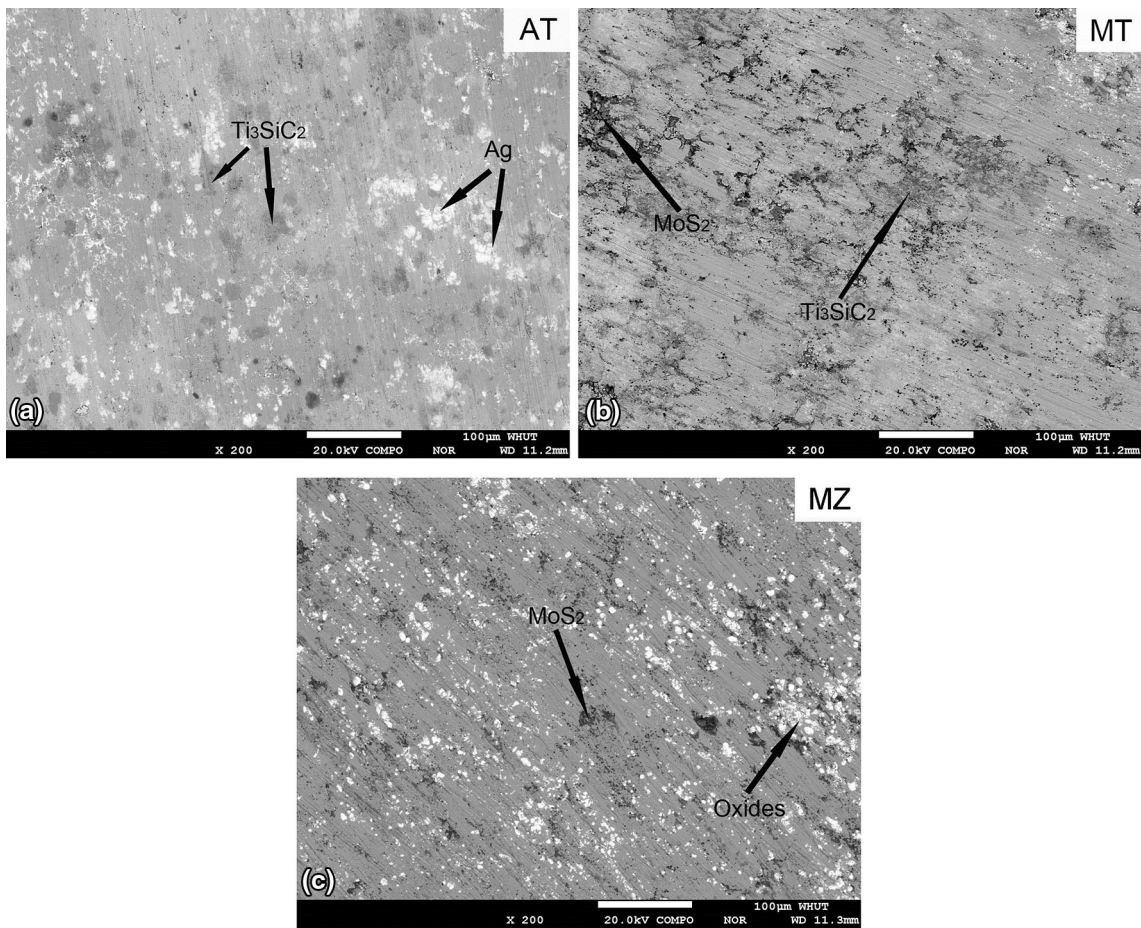


Fig. 3 BEI images of surfaces of the AT, MT, and MZ

the friction by diffusing to the sliding surface and providing easy to shear junctions at the sliding interface (Ref 13). At 600 °C, lots of wear particles and fine grooves on the smooth worn surface indicate that the main wear mechanism could be microplowing. EDS results indicate that Ti-Al-Oxides are formed on the worn surface due to oxidation at high temperature. However, at the testing temperature of 800 °C, the coarse grooves and plastic flow break down the smooth surfaces of AT as shown in Fig. 6(e), which could cause the increase in friction coefficient (see Fig. 4a). At higher temperatures, it may be supposed that Ti_3SiC_2 , being a well known high-temperature lubricant, might have played a greater role in promoting the tribological performance as silver has not been found effective beyond 500 °C (Ref 13). The oxidation protection film of TiO_2 or mixture of TiO_2 and SiO_2 could be formed during the oxidation behavior of Ti_3SiC_2 (Ref 24).

Figure 7 shows the wear track morphologies of MZ tested at different temperatures. As shown in Fig. 7(a), some finer pits and milder scratches are located on the worn surface, if compared to that in Fig. 6(a). It explains that MZ has lower wear rate than AT at RT. The same phenomenon was also observed by Purcek et al. (Ref 25). The fine grooves and some loose particles are present on the relatively smooth worn surface of MZ at 200 °C, as shown in Fig. 7(b), which is different from the pits of AT at RT. It implies that the addition of the MoS_2 lubricant improves the tribological performance when the temperature rises to 200 °C. However, it is clear that

MZ expresses the delamination pits and more loose particles at 400 °C, which could cause a relatively high friction coefficient if compared to the MZ at 200 °C (see Fig. 4a). As shown in Fig. 7(d), the plastic flow traces and some grooves appear on the surface friction layer, which are consistent with the sliding direction; it also shows that the thin tribo-layers are well formed on the worn surface. EDS analysis results of worn surface of MZ obtained at 600 °C show that the relatively bright areas of tribo-layer are the Al-Zn-Oxides. This illustrates that the plastic deformation accompanied by abrasive wear and oxidation wear dominates the wear process of MZ at 600 °C. The smooth tribo-layer consisting of Al-Zn-Oxides as high-temperature solid lubricants provides an excellent self-lubricating property and a favorable anti-wear performance. The ZnO addition helps the formation of Al-Zn-Oxides to act as the anti-wear layers on the worn surface. Bi et al. (Ref 26) also found that NiAl matrix composite with addition of ZnO showed excellent wear resistance at high temperature. According to Fig. 7(e), the MZ at 800 °C exhibits similar surface appearance with plastic deformation including extrusions and grooves, suggesting that the main wear mechanisms are plastic deformation and abrasive wear.

Figure 8 shows the wear track morphologies of MT tested at different temperatures. In sharp contrast to the worn surfaces of the AT and MZ, the tribo-layer and some small scratches are observed on the worn surface of MT at RT (see Fig. 8a), and the dendrite microstructures that are distributed around the

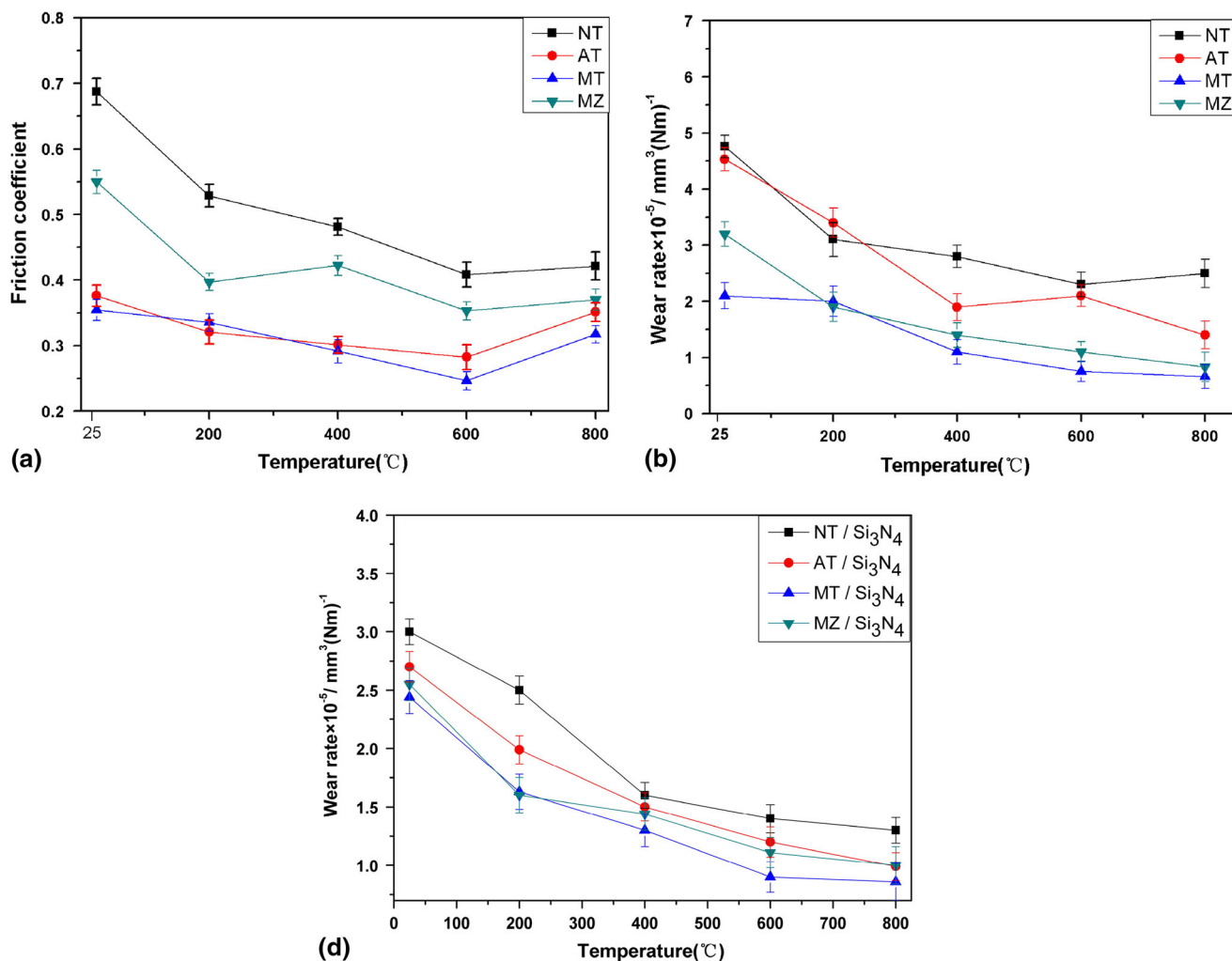


Fig. 4 Variations of friction coefficients (a); wear rates (b) of samples and wear rates of counterface balls at different temperatures (c)

scratches can still be recognized. EDS analysis on the dendrite microstructures show apparent signals of oxides. Due to the tribo-layer of the worn surface and the small scratches, it is highly probable that they could improve the tribological behavior (Ref 26). When the temperature rises to 200 °C, the worn surface exhibits abrasion marks characterized by scratches and deep grooves produced by micro-cutting process (see Fig. 8b). Similar morphology is found on the worn surface of AT at 200 °C. Therefore, the AT and MT have the similar friction coefficients in the range of 0.33-0.34 at 200 °C. Moreover, it is clear that the MT expresses the mild scratches and shallow grooves at 400 °C. According to Fig. 4(b), the MT shows lower wear rate, if compared to the MT at 200 °C. The results show that the addition of MoS₂ lubricant can improve the tribological properties of the MT at relatively low temperatures. MoS₂ as a solid lubricant has been extensively investigated, and the results show that MoS₂ can work well at low temperatures (Ref 15, 16). Furthermore, as shown in Fig. 8(d), the plastic flow traces and some shallow grooves appear on the surface friction layer, which are consistent with the sliding direction; it also shows that the tribo-layers are well formed on the worn surface. EDS analysis results show that the Ti₃SiC₂ lubrication phases are uniformly distributed throughout

the entire worn surface. Combining with the results in Fig. 4(a) and (b), it can be found that the addition of Ti₃SiC₂ lubricant can decrease the friction coefficient and wear rate at relatively high temperatures. Ti₃SiC₂ ceramic exhibits rather low friction coefficient during dry sliding because of the formation of self-lubricating films (Ref 9). As the temperature increases up to 800 °C, the obvious scratches and debris particles break down the smooth surfaces. EDS results show that large number of oxides develop on the worn surfaces. The wear mechanisms are mainly abrasive wear and oxidation wear.

4. Discussion

From the above aforementioned results, the wear mechanisms corresponding with tribological properties change with addition of different lubricants. From the tribological perspective, the wear and self-lubricating mechanisms are inseparable characteristics. In order to further understand the effect of different lubrication phases on wear and lubrication mechanisms, the discussion in this paper focuses on the distinct subsurface microstructure of wear scar of the AT, MZ, and MT

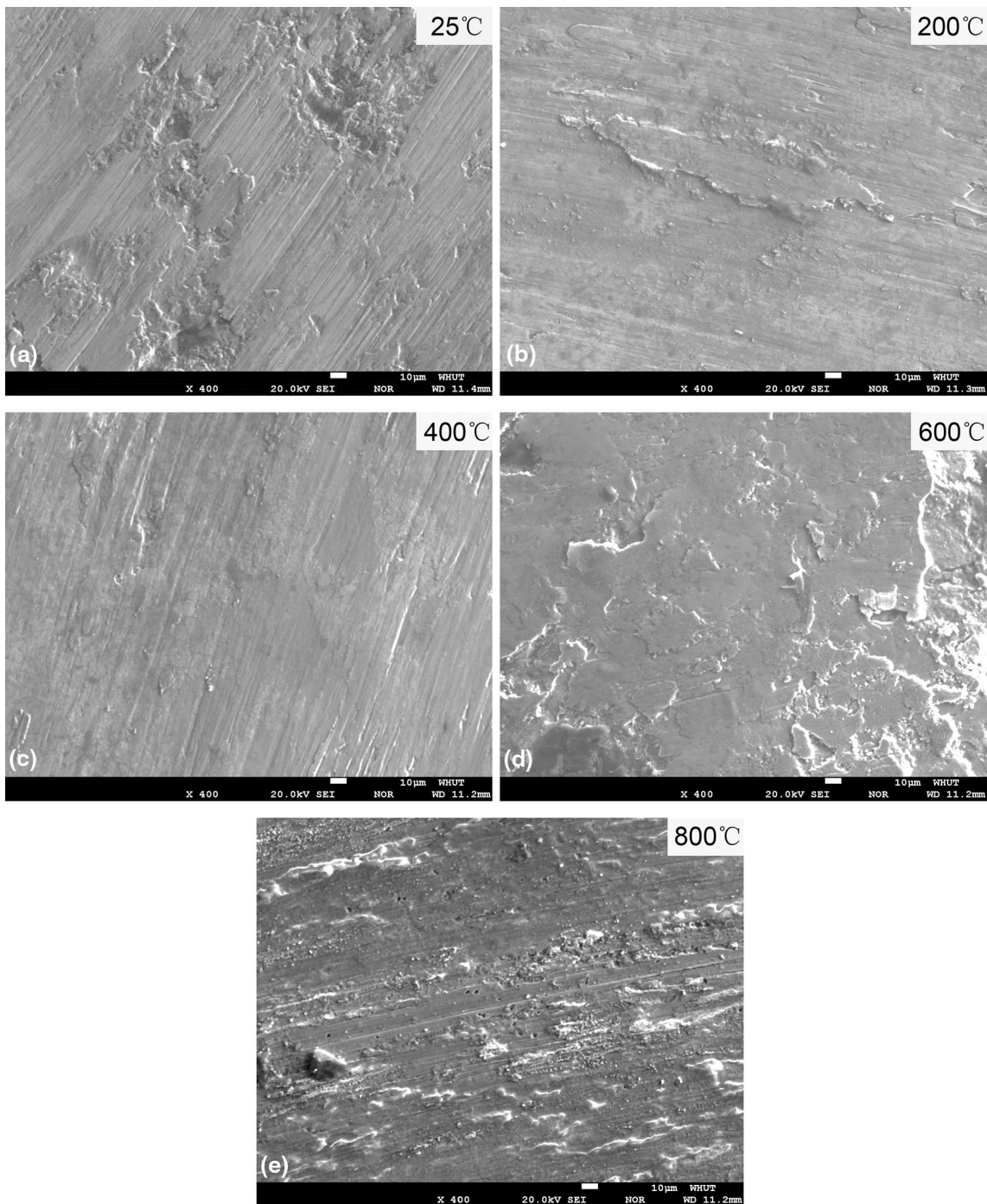


Fig. 5 SEI images of worn surfaces of the NT against Si_3N_4 ball at different temperatures

sliding against the Si_3N_4 ball. The lubrication mechanism of the counterface of MT against Si_3N_4 ball is especially discussed in detail.

4.1 Wear Characteristics of the AT

The wear tracks on the worn surfaces surprisingly show the parallel ridges and deep grooves on the worn surface at the lower temperatures; while the coarse grooves and plastic flow at the higher temperatures. This is to be expected that, with the soft lubricant of Ag addition, the AT has a considerably lower

hardness (7.1 GPa) than that of Si_3N_4 ball (15 GPa). At the onset of a wear process and under the applied contact pressure, since the surface of AT when compared with hard protrusions on the Si_3N_4 ball surface is softer, some protruding particles penetrate into the softer surface of AT and remove the materials of AT by such mechanisms as microploving commonly encountered in abrasive wear. At the same time, wear of Si_3N_4 ball occurs probably due to the brittleness of silicon nitride. Protruding particles of Si_3N_4 ball embedded in the surface of AT produce brittle fracture. This has changed the major wear mechanism from two-body abrasion to three-body

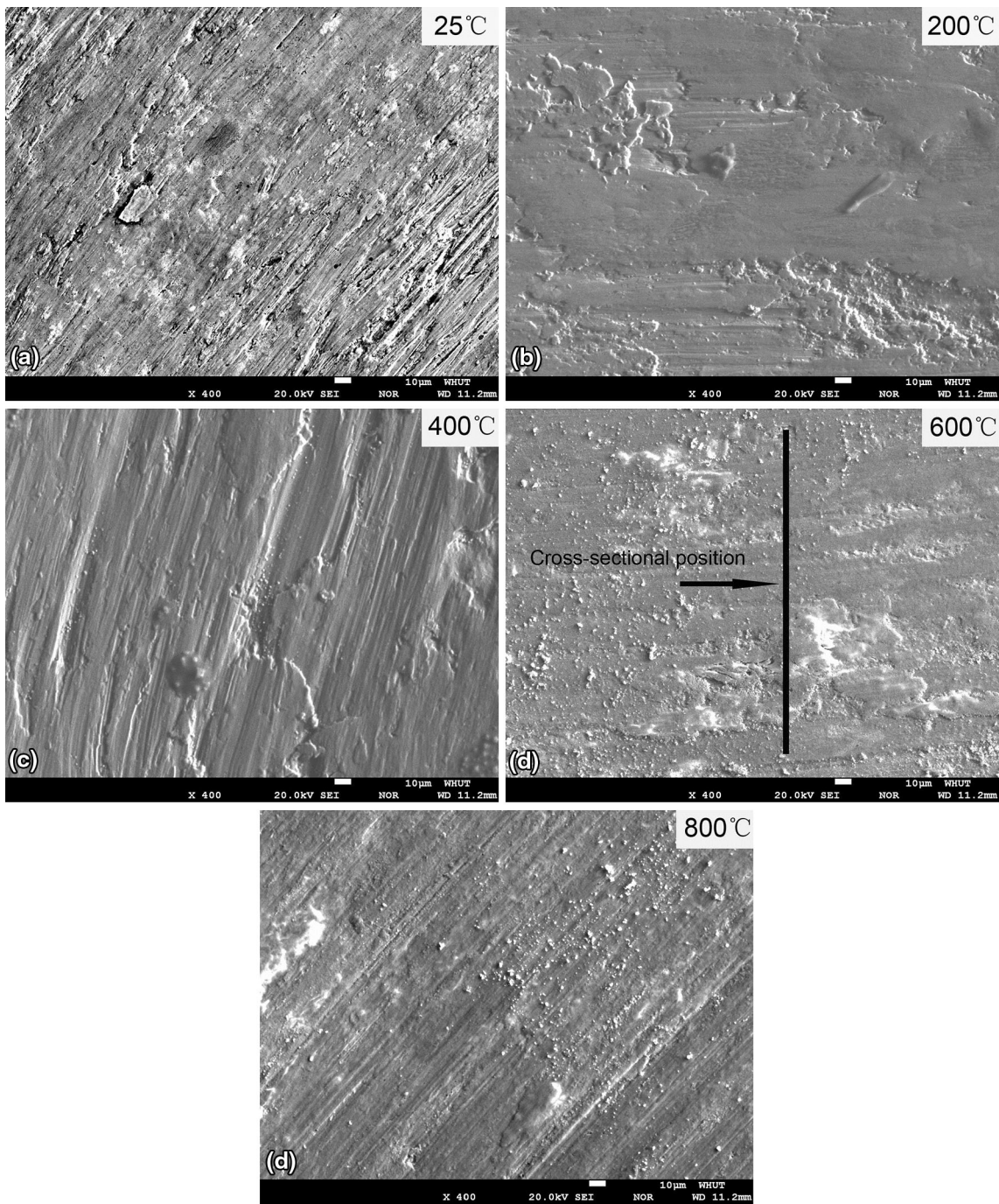


Fig. 6 SEI images of worn surfaces of the AT against Si_3N_4 ball at different temperatures

abrasion. Patched wear debris moving along with the Si_3N_4 ball slider produce the wide ridges and grooves by plowing; and the hard silicon nitride particles in the debris produce scratches by micro-cutting (Ref 27). Due to severe abrasions, the wear rate of AT at lower temperatures is very high, as shown in Fig. 4(b). At high temperatures (above 600 °C), the higher load-carried capacity of Ni_3Al and the lubricity of Ti_3SiC_2 allow AT to provide the lower friction coefficients and wear rates. Additionally, the tribo-layers are produced in the contact surface and cause plastic deformation in the wear track. This can be judged from two reasons. One is that the plastic flow traces and some shallow grooves appear on the surface friction layer of AT,

which are consistent with the sliding direction (see Fig. 6d). Under an applied contact force of 10 N at 600 °C, the contact stress could be above the yield strength of Ni_3Al . The other is that the wear mechanism transfers from two-body abrasion to three-body abrasion, which could result in the tribo-films. In Chuang et al. (Ref 28) it is reported that the three-body contact can lead to physical and chemical interactions, as well as the formation of tribo-films.

In order to clarify the structure and the formation mechanism of the friction layer at 600 °C, the subsurface analysis is carried out on the worn surface of AT by cross-sectioning it perpendicular to the sliding direction, and the location of the

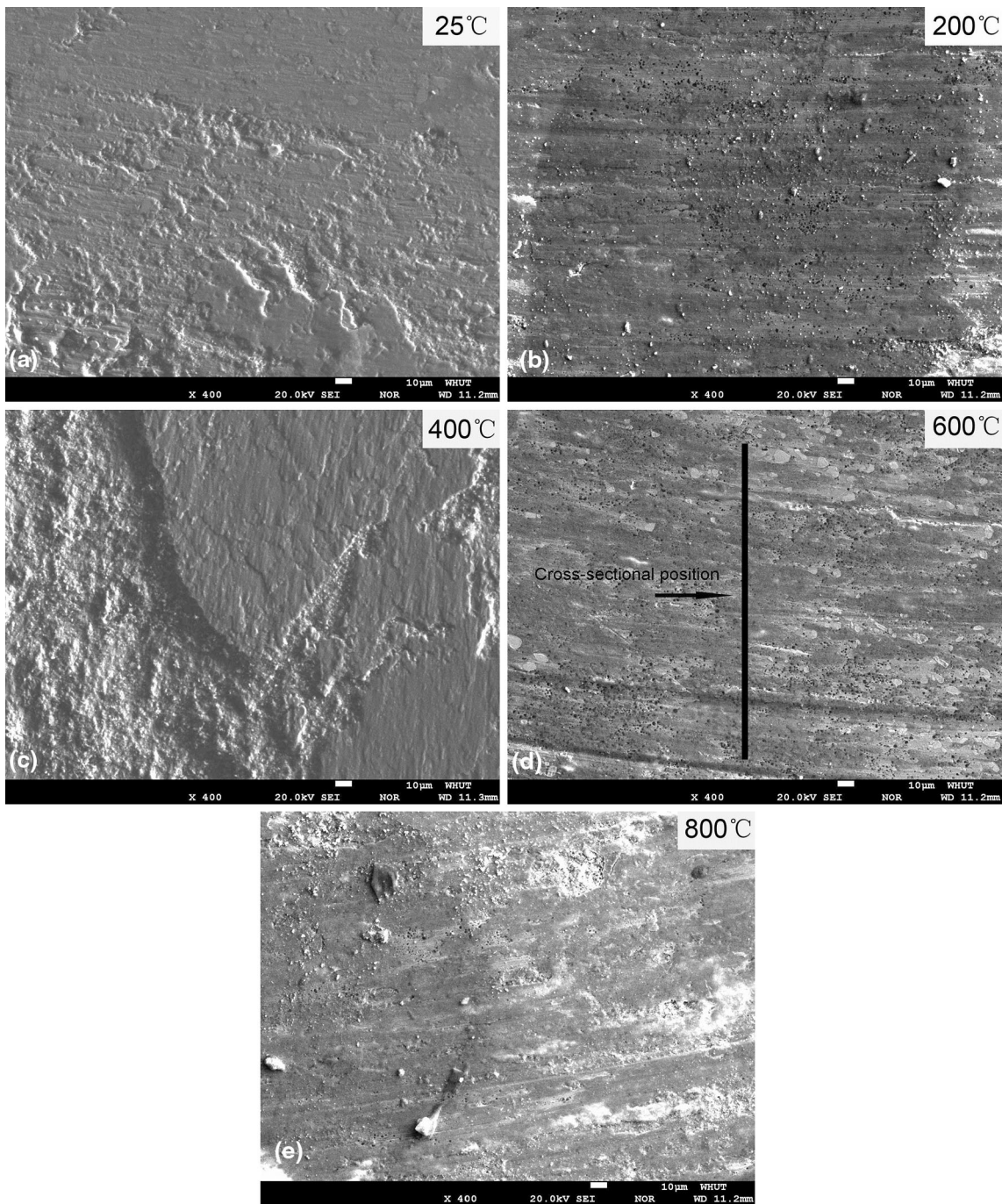


Fig. 7 SEI images of worn surfaces of the MZ against Si_3N_4 ball at different temperatures

cross-sectional position is shown in Fig. 6(d). Figure 9(a) shows the typical SEM micrograph of cross-section of wear scar of AT at 600 °C. Figure 9(b) shows high magnification cross-sectional SEM image of area A taken from the top of the cross-section. As shown in Fig. 9(a), the different morphologies are easily identified. To further analyze this phenomenon, magnification observation has been performed, which reveals the existence of covering layer and mechanically mixed region (see Fig. 9b). EDS analysis shows that average chemical composition (at.%) of the covering layer is 35.21%O-20.68%Al-15.56%Ti-21.30%Ni-1.79%Si-3.31%Cr-2.15%Ag and qualitatively in good agreement with the phase

prediction of the Ti-Al-Oxides and lubricants, which is identical to the result as discussed before. Moreover, subsurface voids, which give rise to crack initiation upon the role of cyclic extrusion stress (see Fig. 9b), are apparent beneath the covering layer. Moreover, the covering layer itself is brittle due to a very high oxide content, which in turn promotes localized failure, and thus splits from the surface. Some wear debris containing lubrication phase and detached particles from covering layer are generated. Soft lubrication phase and a small amount of wear debris are uniformly spread on the worn surface as the mechanically mixed region (see Fig. 9b). The exposed AT surface may then reform a covering layer and

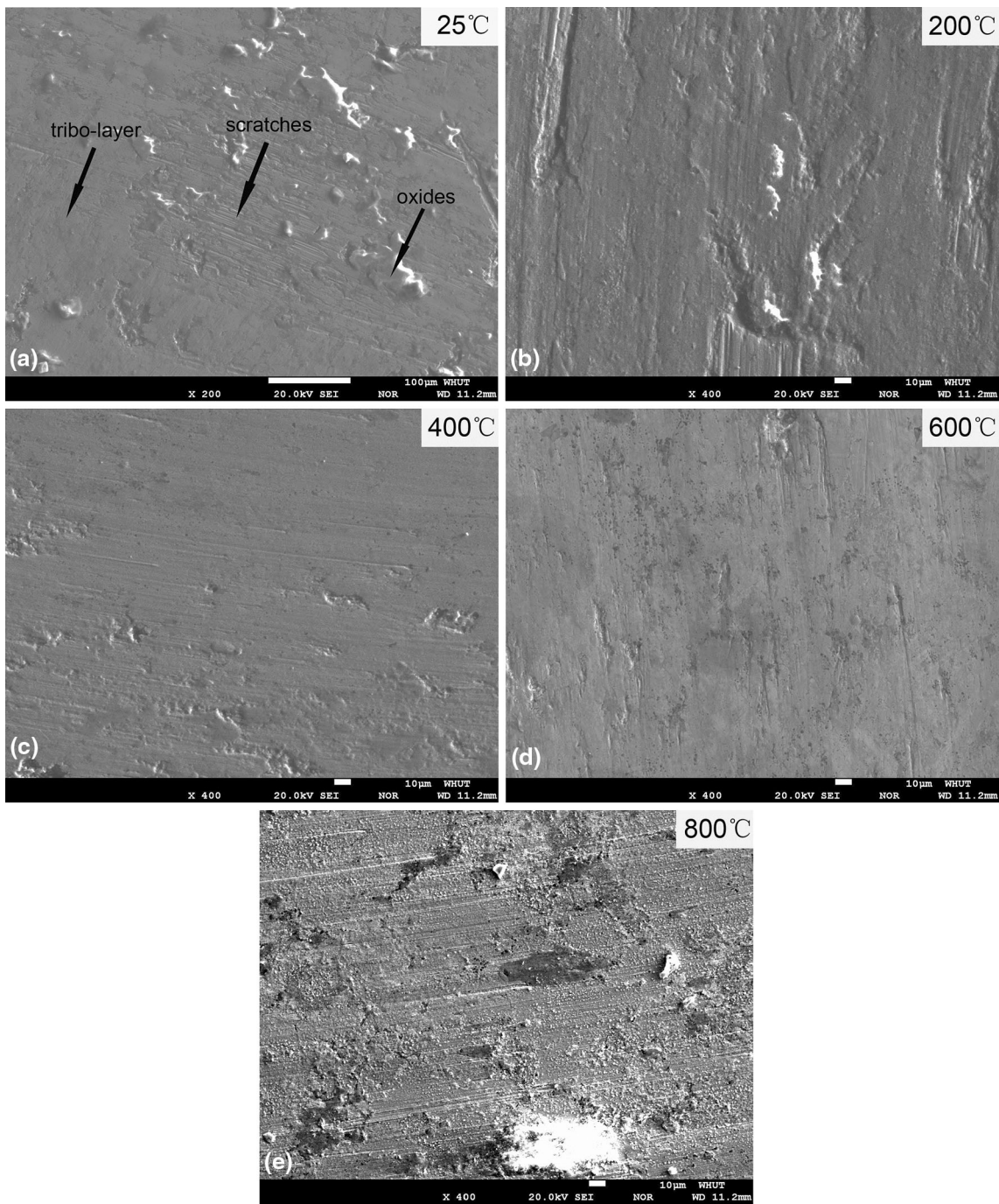


Fig. 8 SEI images of worn surfaces of the MT against Si_3N_4 ball at different temperatures

a mechanically mixed region. This leads to a continuous removal and re-formation of the passivating layer and results in gradual consumption of the AT during sliding (Ref 29). Thus, the covering dynamically and mechanically mixed region formed on the AT sample surfaces does not provide enough protection against wear at 600 °C, resulting in emerging wear particles and fine grooves on the worn surface, which is in good agreement with the wear mechanisms. Hence, the wear rate at 600 °C rises slightly if compared to the wear rates at 400 and 800 °C (see Fig. 4b). However, there

is no denying that the addition of Ag and Ti_3SiC_2 obviously reduces the friction coefficient and wear rate of NT over a wide temperature range.

4.2 Wear Characteristics of the MZ

The friction and wear test results show that there are significant differences in the friction coefficients and wear rates of MZ and NT from RT to 800 °C (see Fig. 4a, b). In other words, the tribological property of MZ has been improved by

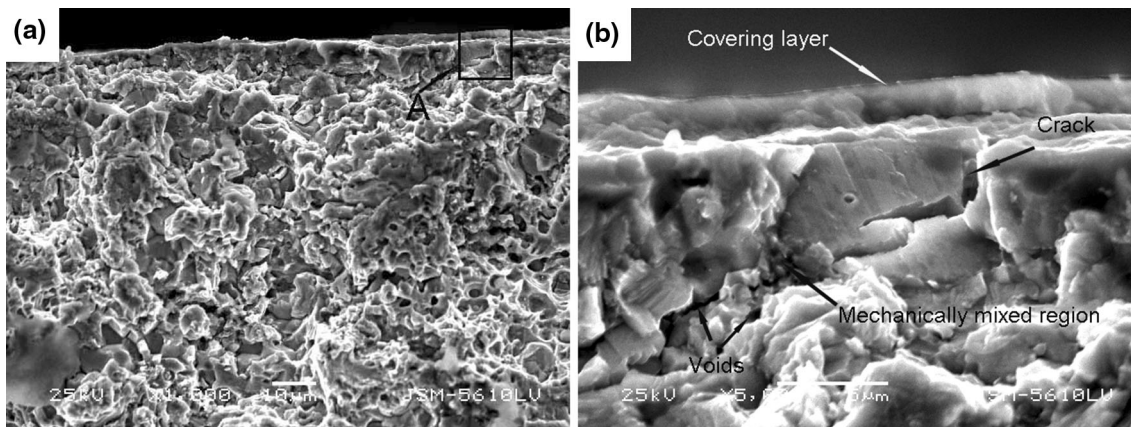


Fig. 9 Typical SEM micrographs showing subsurface microstructure of the AT on cross-section of wear scar after sliding against Si_3N_4 ball at 600°C [(a) SEM image of the friction microstructure; (b) high magnification image (a)]

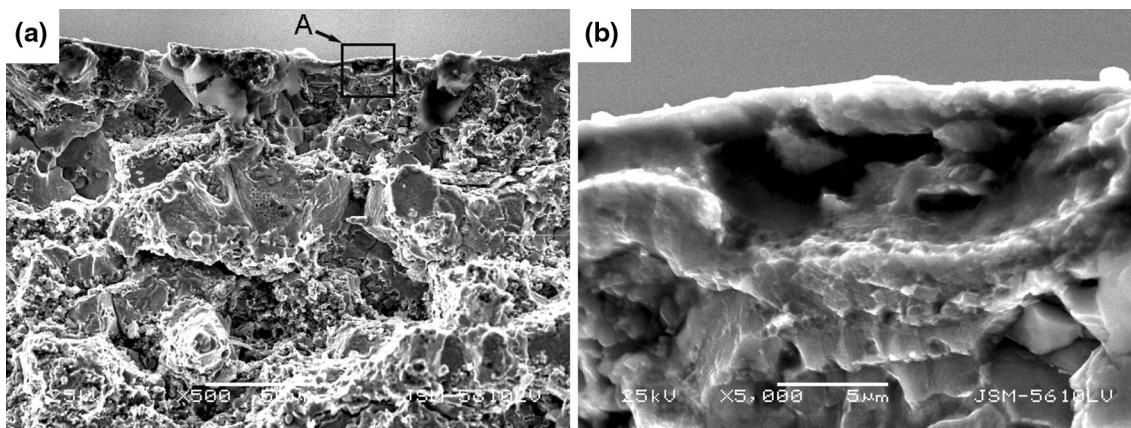


Fig. 10 Typical SEM micrographs showing subsurface microstructure of the MZ on cross-section of wear scar after sliding against Si_3N_4 ball at 600°C [(a) SEM image of the friction microstructure; (b) high magnification image (a)]

adding MoS_2 and ZnO lubricants. This result can be rationalized with the help of the wear mechanisms operating in MZ during dry sliding, such as plastic deformation, oxidation, and abrasive wear, clearly seen on the worn surfaces (see Fig. 7). Among them, the plastic deformation is the dominant wear mechanism. The low friction coefficients and wear rates of the MZ (Fig. 4a, b) are in good agreement with the morphologies of the worn surfaces. At relatively low temperatures, the fine grooves and some loose particles are easily distinguished, and the abrasive wear is the dominant mechanism. The friction coefficients and the wear rates are relatively high, if compared to that at high temperatures. To further investigate the wear mechanisms, subsurface microstructures beneath the worn surface of the MZ perpendicular to the sliding direction at 600°C are studied, and the location of the cross-sectional position is shown in Fig. 7(d). Figure 10(a) shows the typical SEM micrographs of cross-section of wear scar of MZ at 600°C . Figure 10(b) shows high magnification cross-sectional SEM image of area A taken from the top of the cross-section. No evidence of brittle fracture occurs for the MZ due to the unique microstructure of the sample and the outstanding tribological performances of the MZ as aforementioned (as shown in Fig. 7d), while significant subsurface plastic deformation occurs, as shown in Fig. 10(b). As shown in Fig. 10(b),

it can be found that the obvious plastic deformation layer exists at the top of the cross-section. Moreover, beneath the plastic deformation layer, some particles and soft lubrication phase are uniformly spread on the worn surface as the mechanically mixed layer according to EDS analysis. As shown in Fig. 10(a), a relatively black layer exists beneath the plastic deformation layer and the mechanically mixed layer. According to EDS analysis of Fig. 10(a), the black layer is mainly composed of S and Mo elements. On the role of cyclic extrusion stress, the lubrication phase of MoS_2 transfers from the local MZ to worn subsurface and to form the rich-lubrication phase layer at 600°C beneath. Wu et al. (Ref 30) determined that soft nanoparticles were plastically deformed under shear and compression conditions, in contrast to hard nanoparticles. Hence, the plastic deformation occurs at the top of the cross-section due to the enrichment of MoS_2 and ZnO lubricant soft particles. In order to investigate the element enrichment, the x-ray maps of cross-section of the MZ are shown in Fig. 11. According to the x-ray maps, the S, Mo and Zn phases exhibit various degrees of enrichment at the top of the cross-section. Moreover, the x-ray maps surprisingly show that the Si element exists in the cross-section, which transfers from the Si_3N_4 counterface ball to the worn surface of MZ and to form the mechanically mixed layer with some particles and soft

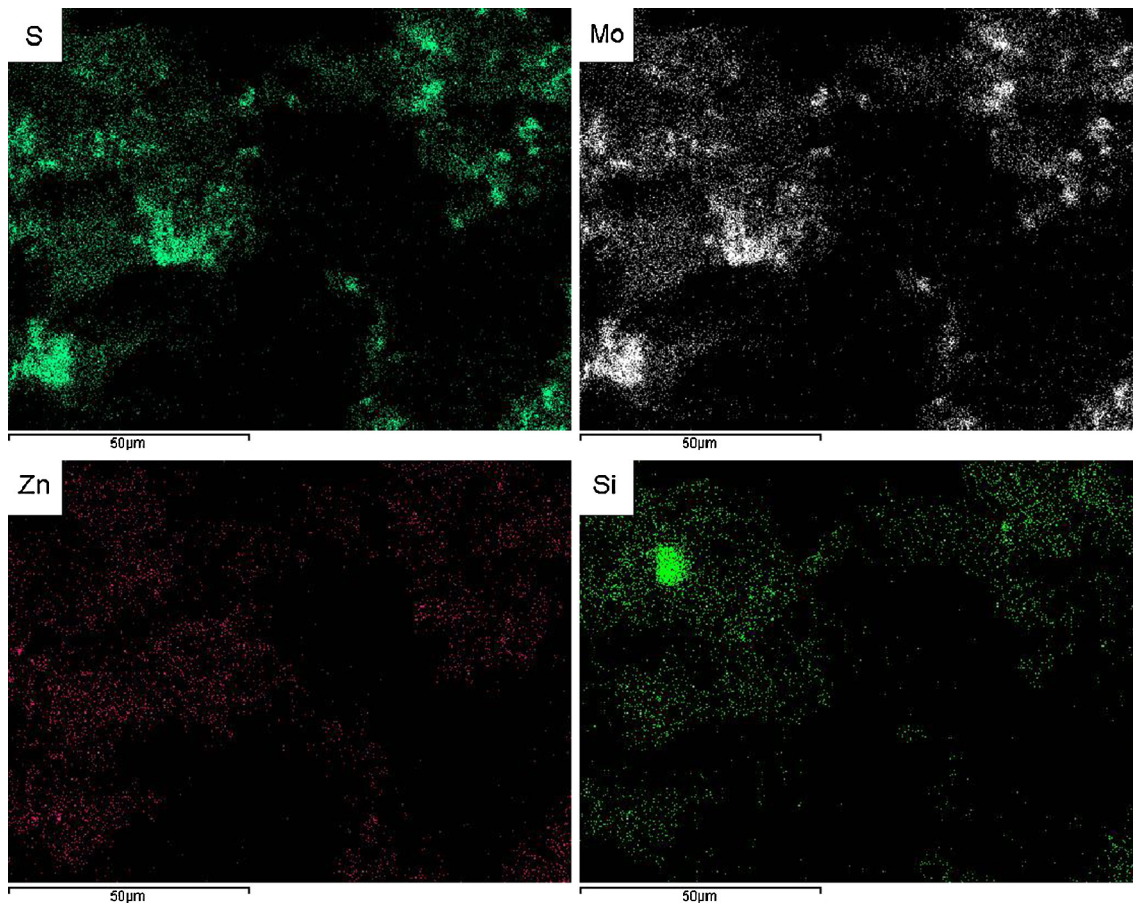


Fig. 11 Elemental distribution of cross-section of wear scar of the MZ against Si_3N_4 ball at 600 °C

lubrication phase. Plastic deformation and changes in structure during early stages of sliding may be precursors to process such as material transfer and mechanical mixing (Ref 31). Our previous study has shown the same phenomenon of the significant stratification morphology (Ref 32). During the sliding friction and wear process, the lubricants can be continuously provided to the friction surface from the rich-lubrication phase layer, which is beneficial to the tribological properties of MZ.

4.3 Wear Characteristics of the MT

Obviously, the MT shows the excellent synergetic lubricating action among the AT, MZ and MT. The MT can be characterized by the low friction coefficients (0.26-0.35) and wear rates ($0.8\text{-}2.1 \times 10^{-5} \text{ mm}^3 \text{ N}^{-1} \text{ m}^{-1}$) over a wide temperature range of 25-800 °C. The excellent tribological properties of the MT are in good agreement with the morphologies of the worn surfaces (see Fig. 8). Morphologies of worn surfaces tested from RT to 600 °C show plastic deformation with relatively smooth surface, which confirm the very low friction coefficients and wear rates. Moreover, the morphology of worn surface tested at 800 °C shows abrasive wear and oxidation wear together with scratches and debris particles, leading to the increase in friction coefficient. In order to clarify the microstructure and the formation mechanism of the friction layer of MT, the subsurface analysis (at RT, 600 and 800 °C) are carried out on the worn surface by cross-sectioning it

perpendicular to the sliding direction. Figure 12 shows the typical SEM micrographs of cross-section of wear scar of the MT after sliding against Si_3N_4 at RT, 600 and 800 °C.

The typical morphologies of site-specific subsurface of the MT at RT are demonstrated in Fig. 12(a) and (b). Figure 12(a) shows the typical stratification morphology of the site-specific subsurface of MT after sliding against Si_3N_4 at RT. Plastic deformation appeared on the surface of the cross-section. Due to the circular sliding of the Si_3N_4 counterface ball on the same wear track of MT at RT, the lubrication phases of MoS_2 and Ti_3SiC_2 start to pile-up at the top of sliding surface, causing the occurrence of plastic deformation. Meanwhile, some wear debris containing plastically deformed lubricating phase and detached particles from dendrite structures are also generated during sliding. As for the role of cyclic extrusion stress, the wear debris with some soft lubrication phases uniformly are spread on the worn surface as the mechanically mixed region with the average size of about 3 μm (see Fig. 12b), which is beneath the plastically deformed region (see Fig. 12a). According to the high magnification image (see Fig. 12b) for area A in Fig. 12(a), good interfacial bonding is observed between the plastically deformed region and the mechanically mixed region, which is necessary for excellent wear resistance. Additionally, in the mechanically mixed region, subsurface voids are also apparent away from the substrate, along with the smaller particles of the mechanically mixed region at the grain boundaries. For the MT at RT, the total depth of the plastically deformed region in other areas is not large (about 2 μm). Voids

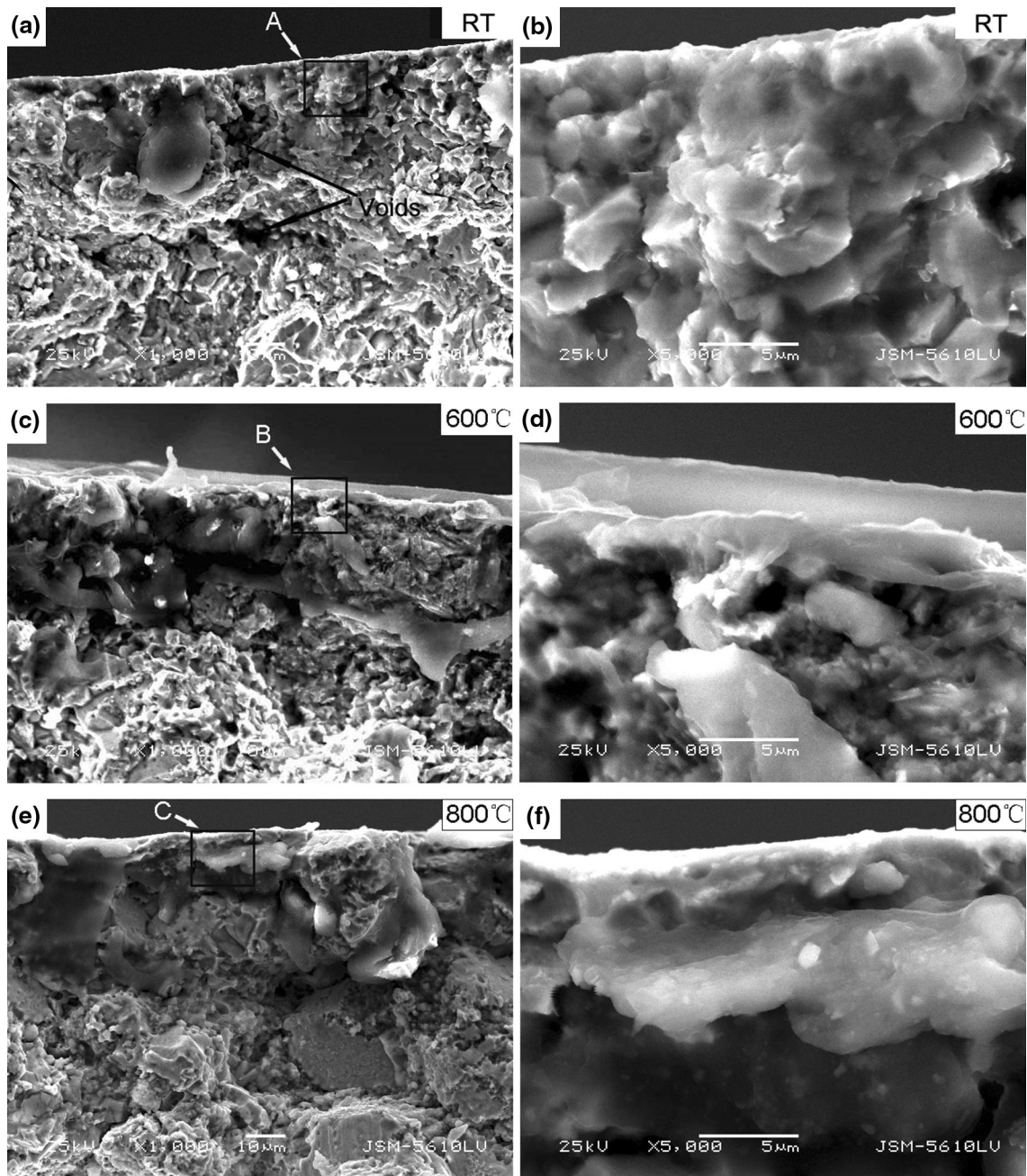


Fig. 12 Typical SEM micrographs showing subsurface microstructure of the MT on cross-sections of wear scars after sliding against Si_3N_4 ball at RT, 600 and 800 °C [(a) SEM image of site-specific subsurface at RT; (b) high magnification image (a); (c) SEM image of site-specific subsurface of at 600 °C; (d) high magnification image (c); (e) SEM image of site-specific subsurface at 800 °C; (f) high magnification image (e)]

within fine grains are present below the plastically deformed region, indicating that the subsurface stress levels are sufficiently high to cause nucleation, but not high enough for void coalescence to form subsurface cracks. Consequently, the MT shows better wear resistance.

The typical morphologies of site-specific subsurface of the MT at 600 °C are demonstrated in Fig. 12(c) and (d), which are distinctly different from the subsurface microstructure of the MT at RT. At 600 °C, the outer worn surface is covered with very smooth self-lubricating films, as shown in Fig. 12(c). Previous study (Ref 33, 34) has shown that the friction is strongly dependent on the presence and properties of

self-lubricating films, as the interfacial shear strength of the film will be a strong contributor to the resistance to motion. Hence, the difference in tribological properties between RT and 600 °C could be attributed to the microstructure of the smooth self-lubricating films. The high magnification image (Fig. 12d) for area B in Fig. 12(c) reveals the typical image of the smooth self-lubricating films. According to Fig. 12(d), the thickness of the smooth self-lubricating films is about 4.5 μm . Additionally, some portions of the finer lubricating phase grains directly contacting with the self-lubricating films are very close to the counterfaces, and the number of grains are fractured to the nanoparticles, during the sliding process. As shown in

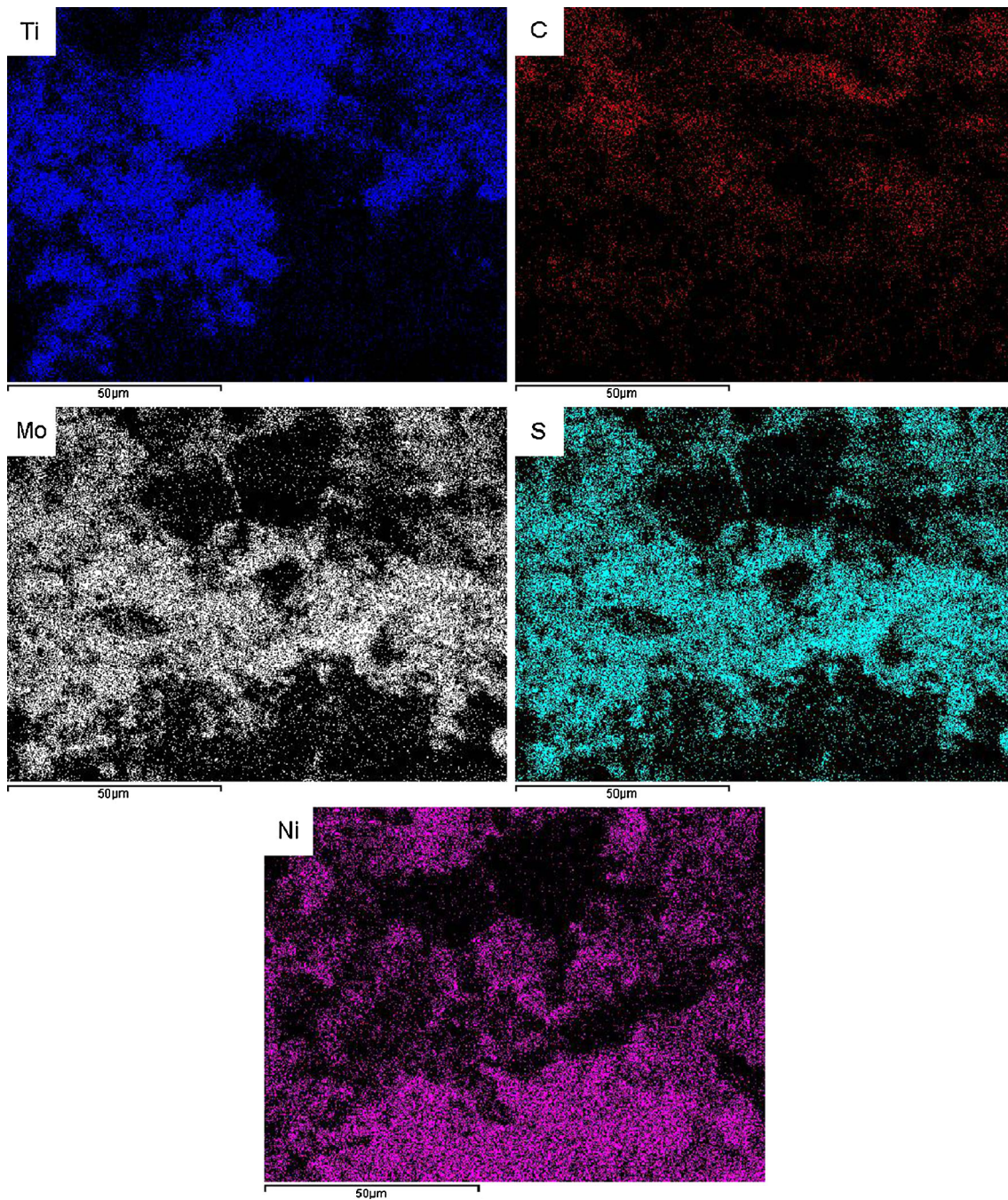


Fig. 13 Elemental distribution of cross-section of wear scar of the MT against Si₃N₄ ball at 800 °C

Fig. 12(d), a nanoparticle layer exists beneath the self-lubricating films. Some soft lubricants and loose particles in the nanoparticle layer are easily plowed and then daubed or smeared on surface of the MT or flaked off directly from the counterface because of the relatively low hardness. Meanwhile, some of detaching transferred fragments between the contact surfaces can be rolled back over the sliding contact surface of the MT under circular further sliding interactions, leading to the formation of smooth self-lubricating films on the MT surface. Due to the self-lubricating films containing soft laminate structure lubricants, it could also be deformed and partly detached from the surface of MT under the combined action of

friction shearing, extrusion stress or cyclic sliding-shearing. Ultimately, the MT, which is covered by the smooth self-lubricating films, exhibits excellent wear resistance and low friction coefficients under the slightly soft-rubbing of the counterface. The contact surface of the MT is shrouded by the self-lubricating films and is almost free from direct contact with the counterpart surface. Moreover, the existence of the self-lubricating films could also prevent the surface of the MT from being directly micro-plowed. Interestingly, some relatively dark area implanting into the nanoparticle layer is found, as shown in Fig. 12(c). EDS analysis for the relatively dark area indicates that the compositions of the relatively dark area are mainly

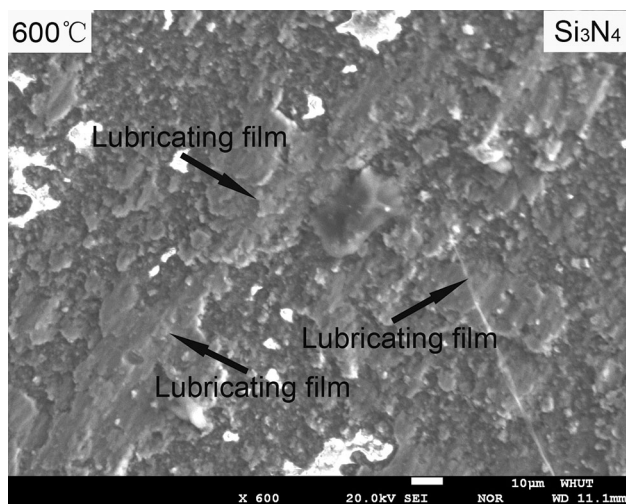


Fig. 14 SEI image of worn surface of Si_3N_4 ball against MT at $600\text{ }^\circ\text{C}$

contain Ti, Si, S and Mo elements, confirming the main compositions are MoS_2 and Ti_3SiC_2 lubricants. On the role of cyclic sliding-shearing, parts of the lubricating phases are fractured to the nanoparticles, which accumulate beneath the self-lubricating films to form the so-called rich-lubrication phase layer. There can be absolutely no doubt about the important role of this rich-lubrication phase layer for the formation of self-lubricating films. In addition, incorporation of MoS_2 and Ti_3SiC_2 significantly reduces the porosity in the subsurface, if compared to RT. The combination of reduced porosity and refined grains is perhaps responsible for the observed decrease in friction coefficient and wear rate in Fig. 4.

The typical morphologies of site-specific subsurface of the MT at $800\text{ }^\circ\text{C}$ are demonstrated in Fig. 12(e) and (f), which are distinctly different from the subsurface microstructure of the MT at $600\text{ }^\circ\text{C}$. Compared with the subsurface microstructure of the MT at $600\text{ }^\circ\text{C}$, no very smooth self-lubricating films are observed at $800\text{ }^\circ\text{C}$, which is in good agreement with the morphology of the worn surface (see Fig. 8e). However, plastic deformation can be observed according to high magnification image (see Fig. 12f) for area c in Fig. 12(e). EDS analysis reveals that most of the plastic deformation area contains oxides, inferring that most plastic deformation areas close to the contacting surface are oxidized, which also is in good agreement with the previous results. Just below this plastic deformation area, the SEM image (see Fig. 12e) shows the presence of sub-micron particles and micron particles that are larger than the nanoparticles in the nanoparticle layer shown in Fig. 12(c) and (d). This particle coarsening is clearly a result of the sliding process at high temperature. Moreover, the mechanism for friction-induced coarsening of particles in the subsurface regions of wear surfaces is perhaps related to phenomenon such as mechanical mixing (Ref 35). In order to further understand the relationship of this phenomenon with the MoS_2 and Ti_3SiC_2 lubricants during sliding process at $800\text{ }^\circ\text{C}$, the x-ray maps close to the cross-section of the MT at $800\text{ }^\circ\text{C}$ are shown in Fig. 13. According to the x-ray maps, the Ti, C, S, Mo and Ni phases exhibit various degrees of layered enrichment on the cross-section of the MT at $800\text{ }^\circ\text{C}$. As shown in Fig. 13, it is reasonable to assume that there are three distinct layers of Ti_3SiC_2 -rich phase, MoS_2 -rich phase and Ni_3Al -rich phase

existing in turn. Ti_3SiC_2 has the same nanolaminate structure like graphite, and also has similar lubrication as graphite (Ref 36, 37). MoS_2 also has the same nanolaminate structure and oxidation/decomposition reactions at high temperatures. Therefore, on the role of cyclic extrusion stress, the lubrication phases of Ti_3SiC_2 and MoS_2 transfers from the local MT to form the distinct layers (as discussed before) at $800\text{ }^\circ\text{C}$. On one hand, the Ti_3SiC_2 and MoS_2 lubricants can be continuously provided to the friction surface from the distinct layers, which is beneficial to the tribological property of the MT. On the other hand, the distinct layered microstructure, in which the MoS_2 -rich phase layer is beneath the Ti_3SiC_2 -rich phase layer, can prevent MoS_2 lubricant from further oxidation/decomposition reactions.

Figure 14 shows the wear track morphology of Si_3N_4 ball against MT at $600\text{ }^\circ\text{C}$. As shown in Fig. 14, the worn surface of Si_3N_4 ball is partly covered with smooth lubricating films, which also exists on worn surface of MT (see Fig. 12d). The films reduce the counter pair contact and provide the low strength junctions in the interface, thus reducing the energy required to shear these junctions and in turn decreasing the friction coefficient (Ref 13).

On the basis of the aforementioned analysis, the MoS_2 and Ti_3SiC_2 lubricants in NMSC show a good synergetic lubricating action over a wide temperature range of $25\text{-}800\text{ }^\circ\text{C}$, and the MT shows both high wear resistance and low friction.

5. Conclusions

The samples show good tribological properties sliding against Si_3N_4 ball over a wide temperature range of $25\text{-}800\text{ }^\circ\text{C}$ due to the synergetic lubricating action of lubricants. The AT shows lower friction coefficients (0.29-0.38), if compared to the MZ (0.38-0.55). The MZ shows lower wear rates ($1.0\text{-}3.2 \times 10^{-5}\text{ mm}^3\text{ N}^{-1}\text{ m}^{-1}$), if compared with the AT ($1.8\text{-}4.5 \times 10^{-5}\text{ mm}^3\text{ N}^{-1}\text{ m}^{-1}$). Moreover, the MT has both the lowest friction coefficients (0.26-0.35) and the lowest wear rates ($0.8\text{-}2.1 \times 10^{-5}\text{ mm}^3\text{ N}^{-1}\text{ m}^{-1}$).

The subsurface microstructures of wear scar of NMSCs change with addition of different lubricants, which have great effects on tribological mechanisms and tribological performances. NMSC with addition of MoS_2 and Ti_3SiC_2 (MT) exhibits distinct subsurface microstructure of wear scar with very smooth self-lubricating films at the top of the cross-section, the nanoparticle layer and rich-lubrication phase layer in turn beneath at the condition of $10\text{ N}\text{-}0.2\text{ m s}^{-1}$ at $600\text{ }^\circ\text{C}$. The contact surface of the MT is shrouded by the self-lubricating films and is almost free from direct contact with the counterpart surface. The existence of the self-lubricating films could also prevent the surface of the MT from being micro-cut or micro-plowed directly, leading to the low friction coefficient of 0.26 and wear rate of $0.9 \times 10^{-5}\text{ mm}^3\text{ N}^{-1}\text{ m}^{-1}$. At RT, there is a good interfacial bonding existing between the distinct plastically deformed region and the mechanically mixed region, resulting in better wear resistance of the MT at RT. At $800\text{ }^\circ\text{C}$, the distinct layered microstructure of the subsurface microstructure of wear scar MT, in which the Ti_3SiC_2 -rich phase layer is above MoS_2 -rich phase layer, leads to the good tribological properties of MT for the lubricating role of Ti_3SiC_2 lubricant at high temperatures. Consequently, the MT has the lowest friction coefficients and wear rates over the wide temperature range of $25\text{-}800\text{ }^\circ\text{C}$.

Acknowledgments

This work was supported by the National Natural Science Foundation of China (51275370); the Nature Science Foundation of Hubei Province (2012FFB05104); the Fundamental Research Funds for the Central Universities (2014-yb-004); the Project for Science and Technology Plan of Wuhan City (2013010501010139); the Academic Leader Program of Wuhan City (201150530146); and the Project for Teaching and Research project of Wuhan University of Technology (2012016). The authors also wish to gratefully thank the Material Research and Testing Center of Wuhan University of Technology for their assistance.

References

1. X.L. Shi, J. Yao, Z.S. Xu, W.Z. Zhai, S.Y. Song, M. Wang, and Q.X. Zhang, Tribological Performance of TiAl Matrix Self-Lubricating Composites Containing Ag, Ti_3SiC_2 and BaF₂/CaF₂ Tested from Room Temperature to 600°C, *Mater. Des.*, 2014, **53**, p 620–633
2. C. Dellacorte, The Effect of Counterface on the Tribological Performance of a High Temperature Solid Lubricant Composite from 25 to 650°C, *Surf. Coat. Technol.*, 1996, **86-87**(2), p 486–492
3. J.H. Ouyang, S. Sasaki, T. Murakami, and K. Umeda, Tribological Properties of Spark-Plasma-Sintered $\text{ZrO}_2(\text{Y}_2\text{O}_3)$ -CaF₂-Ag Composites at Elevated Temperatures, *Wear*, 2005, **258**(9), p 1444–1454
4. H.L. Luo, K. Gong, S.P. Li, C. Xu, X.E. Zhang, F. Di, and C.H. Li, Abrasive Wear Comparison of $\text{Cr}_3\text{C}_2/\text{Ni}_3\text{Al}$ Composite and Stellite 12 Alloy Cladding, *J. Iron Steel Res. Int.*, 2007, **14**(5), p 15–20
5. K. Gong, Z.F. Zhou, P.W. Shum, H.L. Luo, Z.L. Tian, and C.H. Li, Tribological Evaluation on Ni_3Al -Based Alloy and Its Composites Under Unlubricated Wear Condition, *Wear*, 2011, **270**(3-4), p 195–203
6. P.Q. La, Q.J. Xue, and W.M. Liu, Tribological Properties of $\text{Ni}_3\text{Al-Cr}_7\text{C}_3$ Composite Coating Under Water Lubrication, *Tribol. Int.*, 2000, **33**(7), p 469–475
7. S.Y. Zhu, Q.L. Bi, J. Yang, W.M. Li, and Q.J. Xue, Ni_3Al Matrix High Temperature Self-Lubricating Composites, *Tribol. Int.*, 2011, **44**(4), p 445–453
8. S.T. Zhang, J.S. Zhou, B.G. Guo, H.D. Zhou, Y.P. Pu, and J.M. Chen, Preparation and Characterization of Reactively Sintered $\text{Ni}_3\text{Al-hBN-Ag}$ Composite Coating on Ni-Based Superalloy, *J. Alloys Compd.*, 2009, **473**(1-2), p 462–466
9. Y. Zhang, G. Ding, Y. Zhou, and B. Cai, Ti_3SiC_2 -a Self-Lubricating Ceramic, *Mater. Lett.*, 2002, **55**(5), p 285–289
10. A. Souchet, J. Fontaine, M. Belin, T.L. Mogne, J.L. Loubet, and M.W. Barsoum, Tribological Duality of Ti_3SiC_2 , *Tribol. Lett.*, 2005, **18**(3), p 341–352
11. X.L. Shi, M. Wang, Z.S. Xu, W.Z. Zhai, and Q.X. Zhang, Tribological Behavior of $\text{Ti}_3\text{SiC}_2/(\text{WC-10Co})$ Composites Prepared by Spark Plasma Sintering, *Mater. Des.*, 2013, **45**, p 365–376
12. X.L. Shi, M. Wang, W.Z. Zhai, Z.S. Xu, Q.X. Zhang, and Y. Chen, Influence of Ti_3SiC_2 Content on Tribological Properties of NiAl Matrix Self-Lubricating Composites, *Mater. Des.*, 2013, **45**, p 179–189
13. R. Tyagi, D.S. Xiong, J.L. Li, and J.H. Dai, Elevated Temperature Tribological Behavior of Ni Based Composites Containing Nano-Silver and hBN, *Wear*, 2010, **269**(11-12), p 884–890
14. Y.L. Su and W.H. Kao, Tribological Behaviour and Wear Mechanism of MoS_2 -Cr Coatings Sliding Against Various Counterbody, *Tribol. Int.*, 2003, **36**(1), p 11–23
15. K.H. Hu, X.G. Hu, and X.J. Sun, Morphological Effect of MoS_2 Nanoparticles on Catalytic Oxidation and Vacuum Lubrication, *Appl. Surf. Sci.*, 2010, **256**(8), p 2517–2523
16. E. Arslan, Y. Totik, O. Bayrak, I. Efeoglu, and A. Celik, High Temperature Friction and Wear Behavior of MoS_2/Nb Coating in Ambient Air, *J. Coat. Technol. Res.*, 2009, **7**(1), p 131–137
17. M.C. Peng, X.L. Shi, Z.W. Zhu, M. Wang, and Q.X. Zhang, Facile Synthesis of Ti_3SiC_2 Powder by High Energy Ball-Milling and Vacuum Pressureless Heat-Treating Process from Ti-TiC-SiC-Al Powder Mixtures, *Ceram. Int.*, 2012, **38**(3), p 2027–2033
18. ASTM Standards E92-82, *Standard Test Method for Vickers Hardness of Metallic Materials*, ASTM International, West Conshohocken, PA, 2003
19. ASTM Standards G99-95, *Standard Test Method for Wear Testing with a Pin-on-disk Apparatus*, ASTM International, West Conshohocken, PA, 1995
20. K. Gong, H.L. Luo, D. Feng, and C.H. Li, Wear of Ni_3Al -Based Materials and Its Chromium-Carbide Reinforced Composites, *Wear*, 2008, **265**(11-12), p 1751–1755
21. W.Z. Yua, B. Yang, X.M. Chen, W.L. Jiang, Q.C. Yu, and B.Q. Xu, Thermodynamic Calculation and Experimental Investigation on the Products of Carbothermal Reduction of Al_2O_3 Under Vacuum, *Vacuum*, 2012, **86**, p 2005–2009
22. J. Yang, W. Gu, L.M. Pan, K. Song, X. Chen, and T. Qiu, Friction and Wear Properties of In Situ ($\text{TiB}_2 + \text{TiC}$)/ Ti_3SiC_2 Composites, *Wear*, 2011, **271**(11-12), p 2940–2946
23. X. Jia and X.M. Ling, Influence of Al_2O_3 Reinforcement on the Abrasive Wear Characteristic of $\text{Al}_2\text{O}_3/\text{PA1010}$ Composite Coatings, *Wear*, 2005, **258**(9), p 1342–1347
24. B.J. Kooi, R.J. Poppen, N.J.M. Carvalho, J.Th.M. De Hosson, and M.W. Barsoum, Ti_3SiC_2 : A Damage Tolerant Ceramic Studied with Nano-Indentations and Transmission Electron Microscopy, *Acta Mater.*, 2003, **51**(10), p 2859–2872
25. G. Purcek, O. Saray, F. Rubitschek, T. Niendorf, H.J. Maier, and I. Karaman, Effect of Internal Oxidation on Wear Behavior of Ultrafine-Grained Nb-Zr, *Acta Mater.*, 2011, **59**(20), p 7683–7694
26. S.Y. Zhu, Q.L. Bi, M.Y. Niu, J. Yang, and W.M. Liu, Tribological Behavior of NiAl Matrix Composites with Addition of Oxides at High Temperatures, *Wear*, 2012, **274-275**(27), p 423–434
27. C.H. Li, J. Xia, and H. Dong, Sliding wear of TiAl Intermetallics Against Steel and Ceramics of Al_2O_3 , Si_3N_4 and WC/Co, *Wear*, 2006, **261**(5-6), p 693–701
28. M.H. Chuang, M.H. Tsai, W.R. Wang, S.J. Lin, and J.W. Yeh, Microstructure and Wear Behavior of $\text{Al}_x\text{Co}_{1.5}\text{CrFeNi}_{1.5}\text{Ti}_y$ High-Entropy Alloys, *Acta Mater.*, 2011, **59**(16), p 6308–6317
29. J.R. Jiang, F.H. Stott, and M.M. Stack, The Role of Triboparticulates in Dry Sliding Wear, *Tribol. Int.*, 1998, **31**(5), p 245–256
30. J.H. Wu, S. Karthikeyana, M.L. Falk, and D.A. Rigney, Tribological Characteristics of Diamond-Like Carbon (DLC) Based Nanocomposite Coatings, *Wear*, 2005, **205**(1-6), p 744–751
31. H.X. Zhai, Z.Y. Huang, and M.X. Ai, Tribological Behaviors of Bulk Ti_3SiC_2 and Influences of TiC Impurities, *Mater. Sci. Eng. A*, 2006, **435-436**, p 360–370
32. X.L. Shi, W.Z. Zhai, M. Wang, Z.S. Xu, J. Yao, S.Y. Song, Q.D. Abid, and Q.X. Zhang, Tribological Performance of $\text{Ni}_3\text{Al-15 wt}\%\text{Ti}_3\text{SiC}_2$ Composites Against Al_2O_3 , Si_3N_4 and WC-6Co from 25 to 800°C, *Wear*, 2013, **303**(1-2), p 244–254
33. Z. Zhou, W.M. Rainforth, Q. Luo, P.Eh. Hovsepian, J.J. Ojeda, and M.E. Romero-Gonzalez, Wear and Friction of TiAlN/VN Coatings Against Al_2O_3 in Air at Room and Elevated Temperatures, *Acta Mater.*, 2010, **58**(8), p 2912–2925
34. K. Komvopoulos Fellow Ste, S. Pernama, J. Ma, E. Yamaguchi, and P. Ryason, Synergistic Effects of Boron-, Sulfur-, and Phosphorus-Containing Lubricants in Boundary Lubrication of Steel Surfaces, *Tribol. Trans.*, 2005, **48**(2), p 218–229
35. T.W. Scharf, P.G. Kotul, and S.V. Prasad, Friction and Wear Mechanisms in $\text{MoS}_2/\text{Sb}_2\text{O}_3/\text{Au}$ Nanocomposite Coatings, *Acta Mater.*, 2010, **58**(12), p 4100–4109
36. S.F. Ren, J.H. Meng, J.J. Lu, and S.R. Yang, Tribological Behavior of Ti_3SiC_2 Sliding Against Ni-Based Alloys at Elevated Temperatures, *Tribol. Lett.*, 2008, **31**(2), p 129–137
37. X.M. Fan, X.W. Yin, S.S. He, L.T. Zhang, and L.F. Cheng, Friction and Wear Behaviors of C/C-SiC Composites Containing Ti_3SiC_2 , *Wear*, 2012, **274-275**(27), p 188–195